

## *Spitzer* QUASAR AND ULIRG EVOLUTION STUDY (QUEST): II. THE SPECTRAL ENERGY DISTRIBUTIONS OF PALOMAR-GREEN QUASARS

HAGAI NETZER<sup>1</sup> DIETER LUTZ,<sup>2</sup> MARIO SCHWEITZER,<sup>2</sup> ALESSANDRA CONTURSI,<sup>2</sup> ECKHARD STURM,<sup>2</sup> LINDA J. TACCONI,<sup>2</sup>  
 SYLVAIN VEILLEUX,<sup>3</sup> D.-C. KIM,<sup>3</sup> DAVID RUPKE,<sup>3</sup> ANDREW J. BAKER,<sup>4</sup> KALLIOPI DASYRA,<sup>5</sup> JOSEPH MAZZARELLA,<sup>5</sup> STEVEN  
 LORD<sup>6</sup>

*Accepted by ApJ February 1, 2008*

### ABSTRACT

This is the second paper studying the QSOs in the *Spitzer* QUEST sample. Previously we presented new PAH measurements and argued that most of the observed far infrared (FIR) radiation is due to star-forming activity. Here we present spectral energy distributions (SEDs) by supplementing our data with optical, NIR and FIR observations. We define two sub-groups of “weak FIR” and “strong FIR” QSOs, and a third group of FIR non-detections. Assuming a starburst origin for the FIR, we obtain “intrinsic” AGN SEDs by subtracting a starburst template from the mean SEDs. The resulting SEDs are remarkably similar for all groups. They show three distinct peaks corresponding to two silicate emission features and a  $3\mu\text{m}$  bump that we interpret as the signature of the hottest AGN dust. They also display drops beyond  $\sim 20\mu\text{m}$  that we interpret as the signature of the minimum temperature ( $\sim 200$  K) dust. This component must be optically thin to explain the silicate emission and the slope of the long wavelength continuum. We discuss the merits of an alternative model where most of the FIR emission is due to AGN heating. Such models are unlikely to explain the properties of our QSOs but they cannot be ruled out for more luminous objects. We also find correlations between the luminosity at  $5100\text{\AA}$  and two infrared starburst indicators:  $L(60\mu\text{m})$  and  $L(\text{PAH } 7.7\mu\text{m})$ . The correlation of  $L(5100\text{\AA})$  with  $L(60\mu\text{m})$  can be used to measure the relative growth rates and lifetimes of the black hole and the new stars.

*Subject headings:* galaxies: active galaxies: starburst infrared: galaxies quasars: emission lines

### 1. INTRODUCTION

The spectral energy distributions, (SEDs), of active galactic nuclei (AGNs) have been studied, extensively, over various energy bands and for different sub-groups of the AGN population (e.g. Sanders et al. 1989; Elvis et al. 1994, hereafter E94; Scott et al 2004; Haas et al. 2003; Glikman et al. 2006; Richards et al. 2006, [hereafter R06]; Trammell et al 2006). Such studies are essential for estimating the bolometric luminosities of AGNs, for distinguishing between the various sub-classes, and for deriving the relationships between black hole (BH) mass, luminosity and accretion rate. They are also required for understanding the details of the energy production mechanisms at X-ray, UV, optical, infrared (IR) and radio energies. The shape of the observed SED depends on the BH mass and accretion rate, the structure and inclination of the central accretion disk, the presence and the geometry of a dusty central structure, the line of sight absorption and extinction, the presence of luminous starburst regions in the host galaxy and the properties of any central radio source.

The various SED bands can be classified according to the origin of the emitted energy. Here we define “primary radiation” as the part produced within the inner 1000 gravitational

radii (to include the entire central accretion disk). “Secondary radiation” is the energy emitted outside of this radius, due to absorption and reprocessing of primary radiation. The term “intrinsic radiation” will be used to define everything associated with the AGN, i.e. the primary radiation as well as radiation from the vicinity of the BH due to the reprocessing of the primary radiation.

Dust in the immediate vicinity of the central source is known to be a major source of secondary radiation and is probably responsible for most of the emergent near-infrared (NIR) and mid-infrared (MIR) continuum. How much intrinsic AGN-heated dust emission contributes to the far-infrared (FIR) emission spectrum has been an open question for years. This has been discussed extensively in our first paper (Schweitzer et al. 2006, hereafter paper I) where many relevant references are listed, and it is also a major topic of the present work. This is directly related to the possible contribution of star forming (SF) regions to the FIR emission and the maximum and minimum temperatures of the AGN-heated dust.

Most previous studies of AGN SEDs in the MIR, especially those focusing on the more luminous AGNs, were limited by the sensitivity and resolution of earlier MIR instrumentation. This is now changing as new *Spitzer* observations are capable of providing high quality data on larger AGN samples. For example, Lacy et al. (2004) found that detection methods based on MIR colors are efficient tools for selecting all types of AGNs (and also starburst galaxies). The addition of optical colors makes such methods even more efficient (R06). Combinations of optical-MIR colors have been used by Hatziminaoglou et al. (2005) to derive mean type-I SEDs and to investigate the distribution of the bolometric luminosity in small AGN samples. R06 used a much larger sample of 259 Sloan Digital Sky Survey (SDSS) sources, and an optical-

<sup>1</sup> School of Physics and Astronomy and the Wise Observatory, The Raymond and Beverly Sackler Faculty of Exact Sciences, Tel-Aviv University, Tel-Aviv 69978, Israel

<sup>2</sup> Max-Planck-Institut für extraterrestrische Physik, Postfach 1312, 85741 Garching, Germany

<sup>3</sup> Department of Astronomy, University of Maryland, College Park, MD 20742-2421, USA

<sup>4</sup> Department of Physics and Astronomy; Rutgers, the State University of New Jersey; 136 Frelinghuysen Road; Piscataway, NJ 08854-8019.

<sup>5</sup> Spitzer Science Center, 1200 E California Blvd, Pasadena CA 91125

<sup>6</sup> NASA Herschel Science Center, MC 100-22, Caltech, Pasadena CA 91125

MIR color combination, to illustrate the diversity of AGN SEDs and to study the bolometric luminosity and accretion rates in such sources.

The present work is a continuation of our study of the QUEST sample which is described in detail in paper I. In short, we are studying QSOs, ultraluminous infrared galaxies (ULIRGs), and the possible evolutionary connection between the two using *Spitzer*-IRS. The QSO sample is largely drawn from that of Guyon (2002) and Guyon et al. (2006). It consists of Palomar-Green (PG) QSOs and covers the full ranges of bolometric luminosity ( $10^{11.5-13} L_{\odot}$ ), radio loudness, and infrared excess [ $\log(vL_{\nu}(60\mu\text{m})/L_{\text{Bol}} \sim 0.02 - 0.35)$ ] spanned by the local members of the PG QSO sample. The ULIRGs in the sample will be described, in detail, in a forthcoming publication.

Unlike the SED studies mentioned above, we use detailed *Spitzer* spectroscopy that allows us to expand on the earlier broad band work. A major goal of this study is to use MIR spectroscopy in combination with broad band FIR photometry in an attempt to investigate the origin of the FIR emission in intermediate luminosity QSOs. Such objects are classified by R06 as “normal type 1 quasars”. In paper I we focused on PAH features and the correlation of their luminosity with the FIR luminosity of the sources. We detected clear PAH emission in 11 of our sources and argued for their likely presence in most other QSOs. We then used known relationships between PAH emission and star forming activity, and the great similarity of  $L(\text{PAH } 7.7\mu\text{m})/L(60\mu\text{m})$  in QUEST QSOs and the starburst dominated objects among the QUEST ULIRGs, to argue that at least a third and perhaps all of the 50–100  $\mu\text{m}$  luminosity in our QSO sample is due to star formation. Here we present the entire 1–100  $\mu\text{m}$  SED of the QUEST QSOs and use the continuum properties to further investigate the PAH emission as well as other observed MIR features. A major goal is to identify the “pure” or “intrinsic” AGN SED that is produced entirely by the central AGN with no starburst contamination.

Section 2 of the paper presents the MIR continuum spectra of the QSOs in our sample and shows derived SEDs for two sub-groups with weak and strong detected FIR emission, as well as for FIR non-detections. In §3 we introduce the intrinsic AGN-powered SED and discuss the implications for AGN models and the AGN-starburst connection.

## 2. THE INFRARED SED OF QUEST QSOs

### 2.1. *Spitzer* spectra

Our reduction and analysis procedure are described in paper I. The original QUEST sample includes 25 AGNs and four others, with similar properties (IZw 1, PG 1244+026, PG 1448+273 and Mrk 1014) were added from other samples. The data presented here include two QSOs (PG0844+349 and PG0923+201) that were not included in paper I because of their later observation dates. The combined sample now includes a total of 29 QSOs. We use the flux calibrated 6–35  $\mu\text{m}$  spectra and convert them to monochromatic luminosity ( $L_{\lambda}$  erg/sec/Å) using a standard cosmology with  $H_0 = 70 \text{ km s}^{-1} \text{ Mpc}^{-1}$ ,  $\Omega_m = 0.3$  and  $\Omega_{\Lambda} = 0.7$ . Fig. 1 shows the *Spitzer* spectra of these QSOs while the main spectral lines and features are identified in Fig. 2. The spectra are shifted in luminosity to avoid crowding and allow an easier inter-comparison of the overall spectral shape. They are also deredshifted to compare features in the same reference frame. As clearly seen in this diagram, and in several of the diagrams

shown in paper I, there is a large variety of spectral shapes: some objects show a clear increase of  $\lambda L_{\lambda}$  with  $\lambda$  while in others there is a definite change of slope, and a clear decline for  $\lambda > 15\mu\text{m}$ .  $L(60\mu\text{m})/L(15\mu\text{m})$ , a useful measure of the FIR/MIR luminosity ratio, varies by up to a factor of 10 in our sample. The luminosity range in our sample is a factor of about 100 in  $L(15\mu\text{m})$  and does not represent the entire type-I AGN population since very high luminosity sources are missing from the sample. Thus we are not in a position to investigate as large a range of SED properties as done for example in R06. As noted in paper I, most and perhaps all sources show signatures of silicate emissions peaking at around 10 and around 18  $\mu\text{m}$ . These features are the subject of a forthcoming paper.

In what follows we purposely avoid discussing sharp spectral features such as emission lines. These will be discussed in a separate paper. All spectra shown below are presented on a rest wavelength scale to allow easier comparison among sources. For one of the targets shown in Fig. 1 (PG1307+085), the low resolution IRS data down to 5  $\mu\text{m}$  are still proprietary to another program. This source is excluded from much of the subsequent analysis.

### 2.2. NIR and FIR data

The basic *Spitzer* data and the FIR data obtained from the literature for all but two recently observed sources are given in Paper I (table 1). We have supplemented these with NIR data, and FIR data for the two new sources, obtained from the literature. The NIR data were obtained from various sources, in particular Neugebauer et al. (1987) and the 2MASS extended and point source catalogs (Jarrett et al. 2000). Table 1 lists the adopted JHKL fluxes and references, where available. We have also added the optical luminosity, at 5100Å, obtained from the original data of Boroson & Green (1992) and kindly supplied by T. Boroson. As discussed below, this makes an important connection to the primary SED of the sources. Variability may in principle affect the SEDs since many of the optical/near-infrared data were taken about 20 years before the *Spitzer* observations. As for the new FIR data, we followed the procedure in paper I and obtained the luminosity at 60  $\mu\text{m}$  rest wavelength by interpolating the observed fluxes at 60 and 100  $\mu\text{m}$ .  $L(60\mu\text{m})$  is very similar to the standard  $L(\text{FIR})$  used extensively in the literature but relatively robust to cirrus contamination at 100  $\mu\text{m}$  for these faint sources. The FIR luminosities computed this way for the two sources not included in paper I are  $10^{10.38} L_{\odot}$  (PG0844+349) and  $< 10^{11.90} L_{\odot}$  (PG0923+201). Hereafter we assume  $L(\text{FIR})=L(60\mu\text{m})$ .

We extend the IRS spectra to shorter and longer wavelengths by spline interpolations using the photometry obtained from the literature. The dominant sources of uncertainty in this procedure are the photometric uncertainties on the data collected from the literature and the possible continuum variations at short wavelengths since we are using non-simultaneous observations (see also Fig. 4). We also compared our data with the recent Glikman et al. (2006) composite obtained from a sample of 27 AGNs that cover a redshift and luminosity range similar to the QUEST QSOs. Their composite is of higher quality at shorter wavelength and is shown next to our composite SED in Fig. 3.

### 2.3. ‘Strong’, ‘weak’ and non-detected far-infrared sources

To represent the range of far-infrared properties in our sample, we divide the QSOs with FIR detections into ‘strong

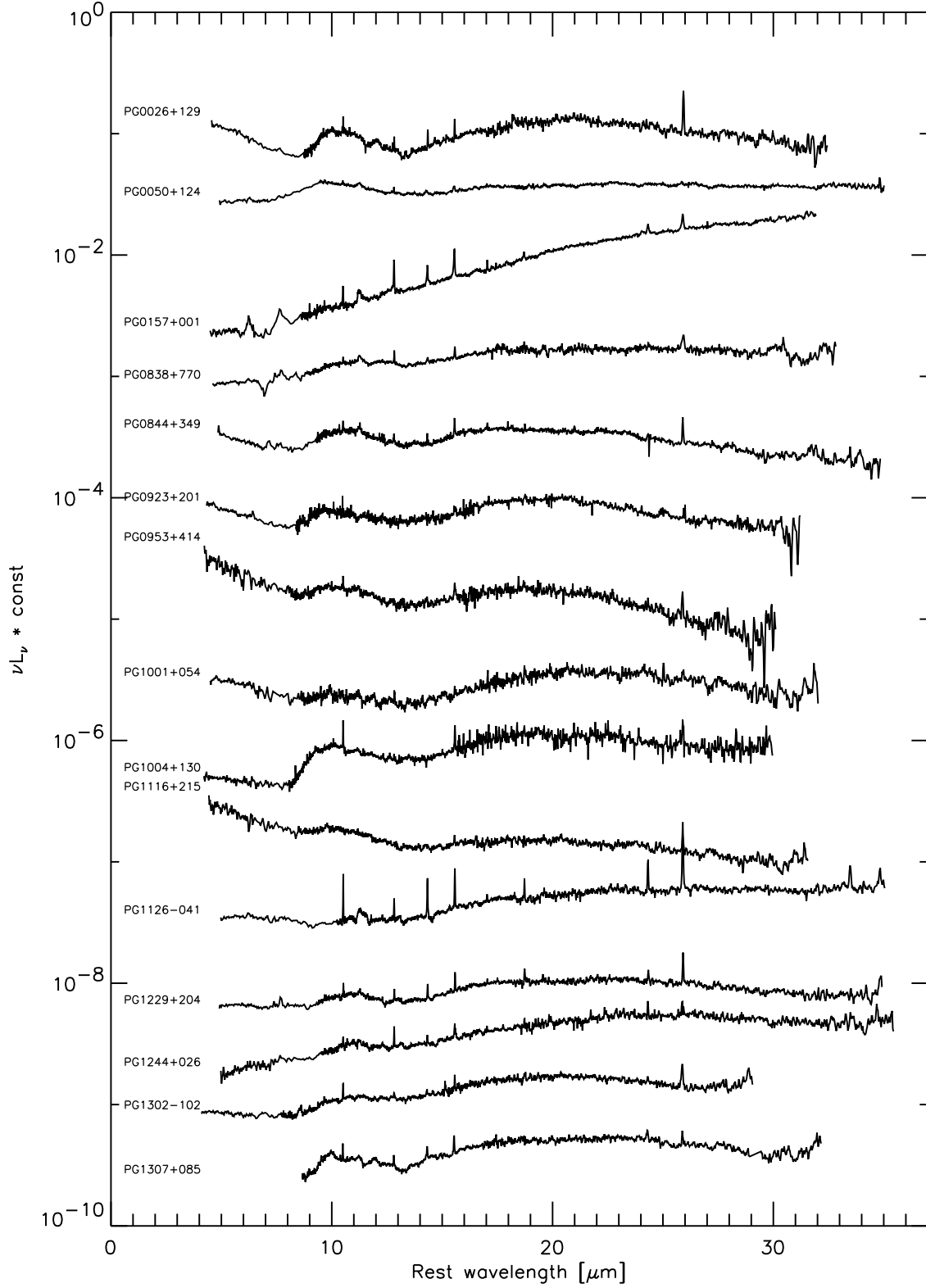


FIG. 1.— IRS spectra of QUEST QSOs de-redshifted to rest-frame wavelengths and given in  $\nu L_\nu$  units. The spectra are shifted vertically to allow clearer view. See Figure 2 for identification of the main spectral features.

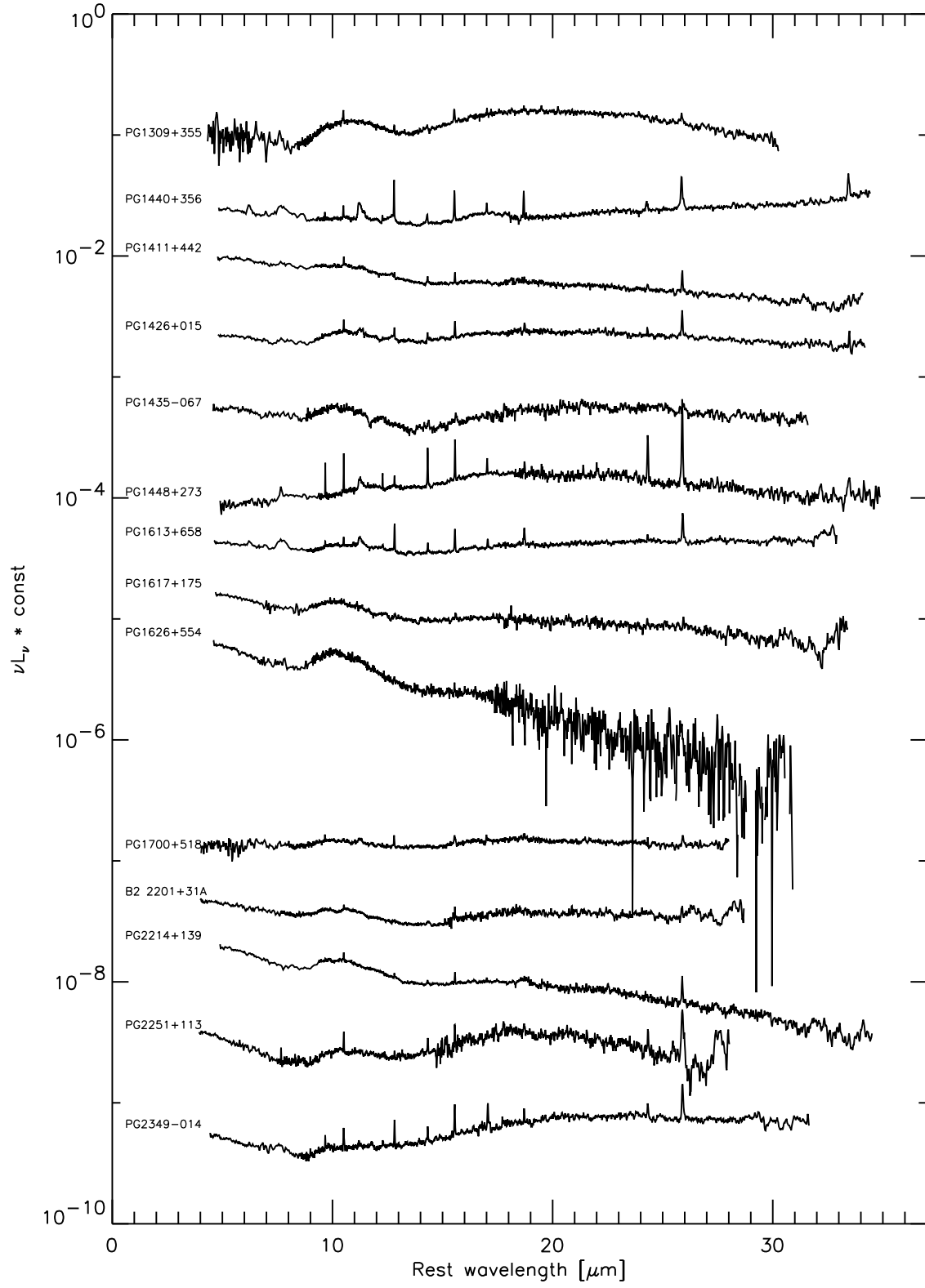


FIG. 1.— continued

TABLE 1  
QSO SAMPLE AND SUPPLEMENTARY DATA

Object	z	Log $L_{5100}$ erg s <sup>-1</sup>	$S_J$ mJy	$S_H$ mJy	$S_K$ mJy	$S_L$ mJy	Refs	FIR class (for plot)
(1)	(2)	(3)	(4)	(5)	(6)	(7)	(8)	(9)
PG0026+129	0.1420	44.66	4.47	5.82	8.51	17.99	N87	undetected
PG0050+124 (IZw1)	0.0611	44.30	21.30	34.40	55.70	127.00	2M,S89	strong
PG0157+001 (Mrk1014)	0.1630	44.67	6.06	7.99	12.70	17.38	2M,N87	strong
PG0838+770	0.1310	44.16	2.29	3.09	4.79	6.31	N87	weak
PG0844+349	0.0640	44.00	6.03	8.51	13.18	23.99	N87	weak
PG0923+201	0.1900	44.89	2.90	4.52	8.79	14.70	2M,S89	undetected
PG0953+414	0.2341	45.11	3.39	4.27	7.76	15.49	N87	undetected
PG1001+054	0.1605	44.25	1.47	2.21	4.10		H82	strong
PG1004+130	0.2400	45.23	4.17	4.27	5.82	9.12	N87	weak
PG1116+215	0.1765	45.13	5.83	8.64	16.15	32.50	2M,S89	undetected
PG1126-041 (Mrk1298)	0.0600	43.82	11.20	16.90	25.00	24.70	2M,S89	strong
PG1229+204 (Mrk771)	0.0630	44.13	6.03	8.51	13.18	23.99	N87	weak
PG1244+026	0.0482	43.26	2.84	3.66	4.79		2M	strong
PG1302-102	0.2784	45.17	3.36	3.77	4.89		H82	strong
PG1307+085	0.1550	44.87	3.55	4.32	6.92	10.32	N87	weak
PG1309+355	0.1840	44.81	3.33	3.63	5.76		2M	undetected
PG1411+442	0.0896	44.31	5.62	8.32	17.38	38.91	N87	weak
PG1426+015	0.0865	44.44	5.89	8.71	15.85	23.44	N87	weak
PG1435-067	0.1260	44.39	2.52	3.23	5.84		2M	strong
PG1440+356 (Mrk478)	0.0791	44.22	9.77	15.14	25.12	38.91	N87	strong
PG1448+273	0.0650	43.99	6.17	8.41	11.89	15.14	N87	weak
PG1613+658 (Mrk876)	0.1290	44.70	4.57	6.31	10.72	17.38	N87	strong
PG1617+175	0.1124	44.29	4.27	6.46	12.30	19.50	N87	undetected
PG1626+554	0.1330	44.44	2.75	3.43	5.68		2M	???
PG1700+518	0.2920	45.68	4.37	6.53	12.74	30.90	N87	weak
B2 2201+31A	0.2950	45.91	2.61	4.24	7.73		2M	undetected
PG2214+139 (Mrk304)	0.0658	44.40	12.20	16.30	22.90	26.30	2M,M83	???
PG2251+113	0.3255	45.63	3.39	4.68	7.24	10.72	N87	undetected
PG2349-014	0.1740	45.21	4.17	5.57	9.55	17.78	N87	strong

NOTE. —

Col. (1) — Source name.

Col. (2) — Redshift.

Cols. (3) — Continuum luminosity  $\lambda L_\lambda$  at 5100Å rest wavelength (from spectra by T. Boroson, priv. comm.).

Cols. (4-8) — near-infrared fluxes in the JHKL observed bands, and related references:

2M — 2MASS magnitudes, extended source catalog (Jarrett et al. 2000) K20 isophotal magnitudes for slightly extended sources, point source catalog magnitudes otherwise;

H82 — Hyland & Allen (1982);

M83 — McAlary et al. (1983);

N87 — Neugebauer et al. (1987);

S89 — Sanders et al. (1989).

Col. (9) — Classification as far-infrared strong/weak (relative to the mid-infrared), or undetected. See text for definition and treatment of PG1626+554 and PG2214+139

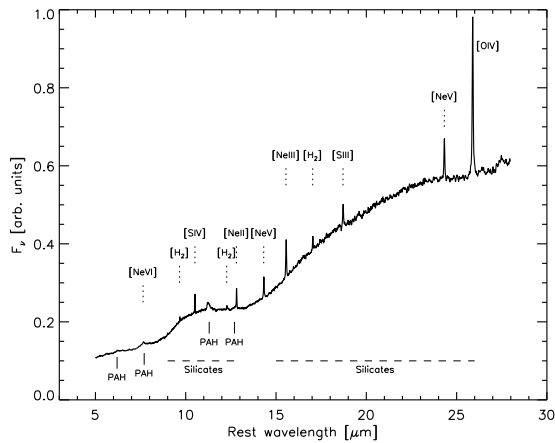


FIG. 2.— Average IRS spectrum of all QSOs except PG1307+085. The main emission lines and features are marked.

FIR' and 'weak FIR' emitters with a dividing line at rest  $L(60\mu\text{m})/L(15\mu\text{m})=1$ . Our definition thus implies 'strong' or 'weak' with respect to the mid-IR emission rather than in

an absolute sense. Out of the 21 QSOs in our sample with detectable FIR flux, two (PG2214+139 and PG1626+554) are problematic since the *Spitzer* spectra show a clear decline of  $\lambda L_\lambda$  from 15 to  $30\mu\text{m}$  yet the  $L(60\mu\text{m})$  point lies clearly above the extrapolation of this spectrum. We suspect that the large aperture FIR data, close to the detection flux limit of the IRAS and ISO instruments, are error-prone so we have chosen to leave those sources out of the analysis. Also excluding PG1307+085, there remain 18 high quality SEDs extending to the FIR, out of which 10 are classified as strong-FIR sources and 8 as weak-FIR sources. The remaining eight sources without FIR detection define a third sub-sample; as explained in Paper I, these are more likely to belong to the class of weak-FIR emitters and to also show very low equivalent width PAH  $7.7\mu\text{m}$  emission, rather than having a rising IR flux but a long wavelength flux below the detection limit. We include the IRS and short wavelength data of those targets where applicable.

Fig. 3 shows the mean SEDs of the full sample (excluding PG1307+085) as well as of the above three FIR subgroups. The relative fluxes of the full SED are given in Table 2. Setting aside emission lines and PAH features, all these mid-

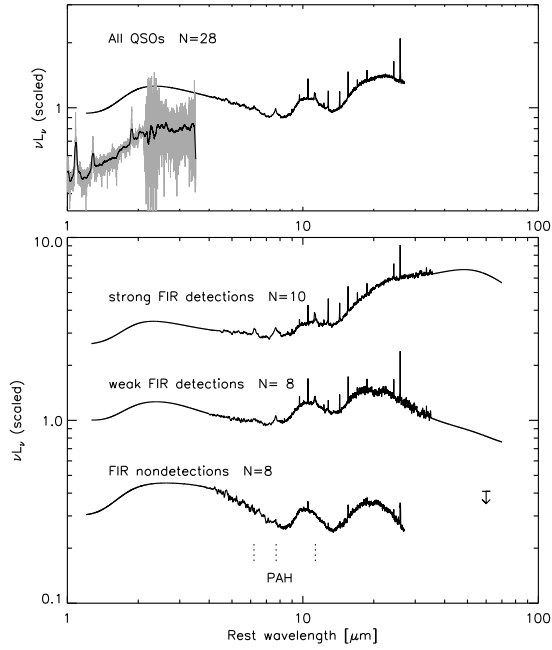


FIG. 3.— Top panel: Average spectral energy distribution for QUEST QSOs in our sample, normalized at  $6\mu\text{m}$ . For comparison, we overplot the mean SED derived from ground-based data at shorter wavelengths for a QSO sample of similar luminosity by Glikman et al. (2006), shifted by an arbitrary amount. Bottom panel: Average SEDs for the three subgroups of strong FIR detections, weak FIR detections, and FIR non-detections. Note the increase of EW(PAH  $7.7\mu\text{m}$ ) from bottom to top.

infrared SEDs show three pronounced peaks: one at  $2\text{--}3\mu\text{m}$  plus the two silicate peaks at  $\sim 10$  and  $\sim 18\mu\text{m}$ . In addition to these components, there is a differing amount of FIR emission according to the specific subgroup. As discussed in paper I, FIR emission and PAH emission from the hosts of PG QSOs are correlated. Indeed, Fig. 3 shows that the equivalent width of PAH  $7.7\mu\text{m}$  varies along with the far-infrared properties of the three subgroups.

The scatter of SED shapes within each group is indicated in Fig. 4. The SEDs clearly show upturns and downturns at long ( $\lambda > 40\mu\text{m}$ ) wavelengths justifying the terms strong and weak FIR sources. However, there is a range of properties within each group and a continuous transition from one to the other. We also show, in thick black lines, the three mean SEDs. We prefer the use of mean rather than median spectra because they better preserve the integrity of features in the SEDs and because of the small number of sources. However, the overall differences between the median and the mean SEDs are not large.

The individual source SEDs sometimes show structure at  $\lambda < 5\mu\text{m}$  which may be due to uncertain (literature) photometry and/or variability. However, the detections of the three peaks noted above in all mean SEDs of Fig. 3 suggest this result is robust.

The results shown here are consistent with the conclusions of paper I that most, and perhaps all QSOs show some level of PAH emission, and that any classifications into PAH-detected and non-PAH-detected categories is likely due to a combination of real differences in EW(PAH  $7.7\mu\text{m}$ ) (or other PAHs) and observational limitations (e.g. aperture effects). It is therefore not surprising that both groups, of strong and weak FIR sources, include sources with detectable PAH  $7.7\mu\text{m}$ . We expect future higher signal-to-noise spectra to reveal currently

non-detected PAHs. In summary, the observations of the QUEST QSOs suggest that we are sampling a distribution in all three properties: PAH luminosity, FIR luminosity and SED shape, with a tendency for larger FIR luminosity sources to have larger  $L(\text{PAH } 7.7\mu\text{m})$  and a long wavelength upturn of their SED.

#### 2.4. Correlations between $L(\text{FIR})$ and $L(\text{PAH})$ and the primary AGN luminosity

So far we have only considered the NIR, MIR and FIR parts of the SED. These are mostly due to thermal emission from cool and hot dust which, by definition, are secondary sources of radiation. Our data set also includes  $4000\text{--}6000\text{\AA}$  spectra of all sources. This radiation is thought to be emitted by the central accretion disk and is thus primary. We can directly compare this radiation with several of the IR components, including those suspected to be of starburst origin. In the following we use  $L(5100)$  to specify  $\lambda L_\lambda$  at  $5100\text{\AA}$ . This quantity is relatively easy to measure and is widely used to derive the BLR size and the central BH hole masses in AGNs (e.g. Kaspi et al. 2005).

The correlation of  $L(5100)$  with  $L(60\mu\text{m})$  is shown in Fig. 5 where we plot data for all the QUEST QSOs (21 detections and 8 upper limits). The diagram exhibits a very strong correlation over more than two orders of magnitudes in  $L(5100)$  with a slope  $\alpha \simeq 0.8$  ( $L(60\mu\text{m}) \propto L(5100)^\alpha$ ) for the  $60\mu\text{m}$  detected sources. The error on the slope is about 0.16, again using only real detections. Assuming the upper limits represent real detections we get a very significant correlation. However, at this stage the result is not very sound since testing for the correlation of the observed fluxes (i.e. the observed  $\lambda f_\lambda$  at  $60\mu\text{m}$  rest wavelength vs.  $\lambda f_\lambda$  at  $5100\text{\AA}$  rest wavelength) gives a much weaker dependence (rank correlation of 98% significance when all sources are included). This is likely the result of the large spread in  $L(\text{FIR})$  and  $L(60\mu\text{m})$  together with the very limited flux range of the sample. A larger sample is required to verify this relationship. Notwithstanding this limitation, we proceed by assuming that the two luminosities are indeed correlated and discuss the implications to AGN physics.

Estimates of the bolometric luminosity,  $L_{\text{bol}}$ , of unreddened AGNs (e.g. Shemmer et al. 2004; Marconi et al. 2004; Netzer & Trakhtenbrot 2007) are 5–10 times larger than  $L(5100)$ . In this context  $L_{\text{bol}}$  applies to the primary continuum radiation and the above references suggest that the bolometric correction is probably luminosity dependent. For the luminosity range of the QUEST QSOs,  $L_{\text{bol}} \sim 7L(5100)$ . This issue is crucial to our work and we need to describe it in more detail.

The multi-wavelength multi-object study by R06 followed the Elvis et al. (1994) approach and recommended a large bolometric correction ( $\sim 12$ ) relative to  $L(5100)$ . The number was obtained by integrating over the entire continuum, including the infrared part. According to our definition, there is a clear distinction between the primary and secondary sources of radiation. The former is the result of the accretion disk and its corona (or alternative X-ray producing mechanism) and the latter is due to reprocessed radiation. The bolometric correction factor of  $\sim 7$  used here assumes isotropic radiation by the primary source at all wavelengths. Under this assumption, the R06 procedure involves double counting and hence the larger bolometric correction factor obtained by these authors. In our sample  $L(\text{FIR})$  is, on the average, very similar to  $L(5100)$  (see Fig. 5). Given the above bolometric correction

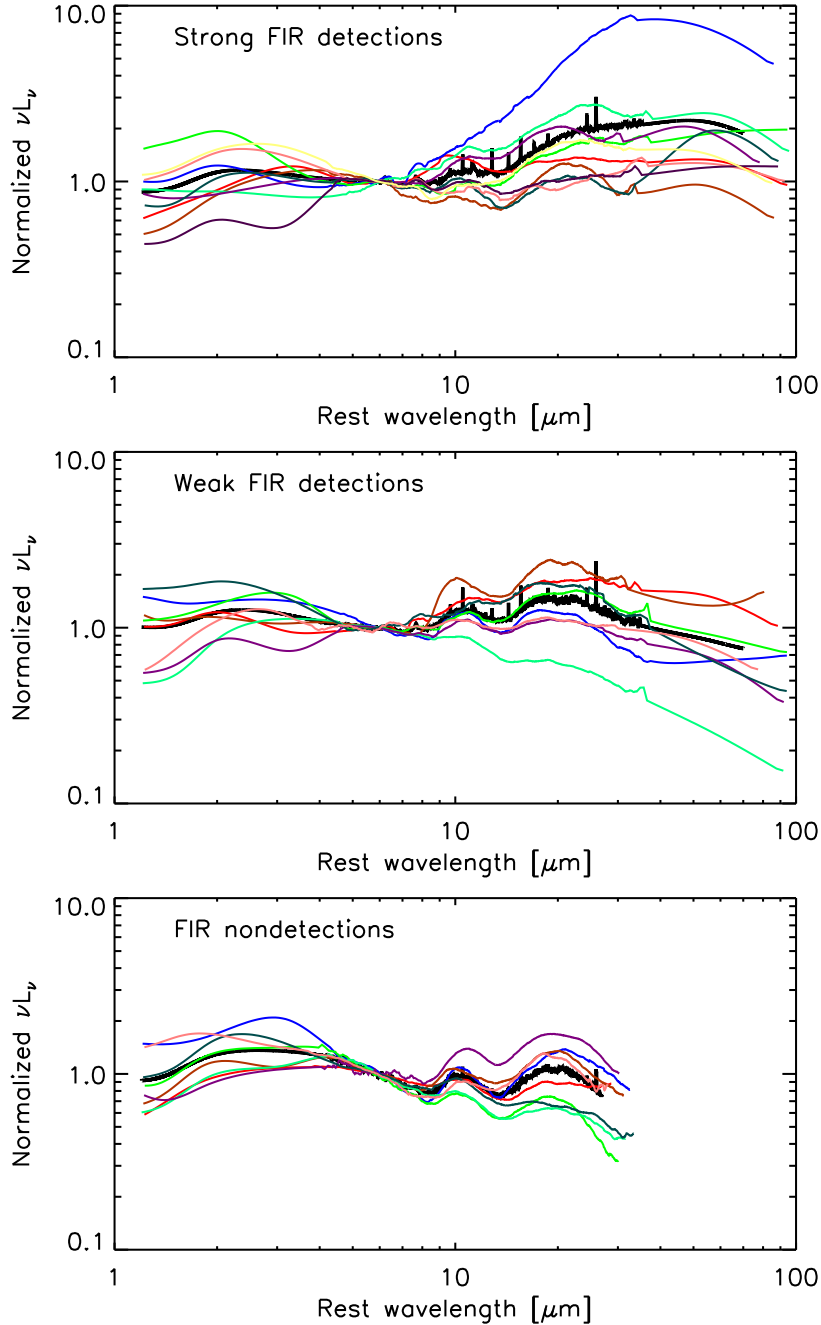


FIG. 4.— SEDs of 10 FIR-strong (top), 8 FIR-weak (middle) and 8 FIR-undetected (bottom) sources. The central  $\sim 5\text{--}35\mu\text{m}$  parts of the curves cover the range of the *Spitzer* IRS spectra which are shown smoothed here. The short wavelength part (optical, J, H, K and L photometry) and the long wavelength IRAS or ISO data have been joined to the IRS spectra by interpolating splines. The black heavy lines are the mean spectra of the two groups already shown in Fig. 3, the colored curves show the scatter of individual objects around this mean. All spectra are normalized at  $6\mu\text{m}$  rest wavelength.

we find that for QUEST QSOs,  $L(\text{FIR})$  is roughly 10–20% of the (primary) AGN bolometric luminosity.

A similar correlation to the one shown in Fig. 5 was also found by Haas et al. (2003) in their study of a large sample of PG QSOs (see Fig. 4 in their paper). That sample contains a small number of sources with optical luminosities that are significantly higher than those considered here. These sources seem to deviate from the almost 1:1 relationship found here with a hint that the FIR luminosity levels off at around  $10^{13}L_{\odot}$ . (Note that Haas et al. use  $L_B$  which is somewhat different than  $L(5100)$  used here).

We also test the correlation of  $L(5100)$  with  $L(\text{PAH } 7.7\mu\text{m})$

which was not available in the Haas et al. (2003) sample. As noted earlier, there are 11 sources with direct  $L(\text{PAH } 7.7\mu\text{m})$  measurements and 17 with upper limits. All are plotted in the lower part of Fig. 5. The diagram suggests a tight correlation between the two properties with the more optically luminous sources also the ones with larger  $L(\text{PAH } 7.7\mu\text{m})$ . This was not investigated statistically since the majority of sources do not have direct PAH detections. The strong correlation is not surprising given the correlations of both  $L(5100)$  and  $L(\text{PAH } 7.7\mu\text{m})$  with  $L(\text{FIR})$  and the fact that most measured upper limits on  $L(\text{PAH } 7.7\mu\text{m})$  are likely to be within a factor of 2–3 of the real  $L(\text{PAH } 7.7\mu\text{m})$  (paper I). While we

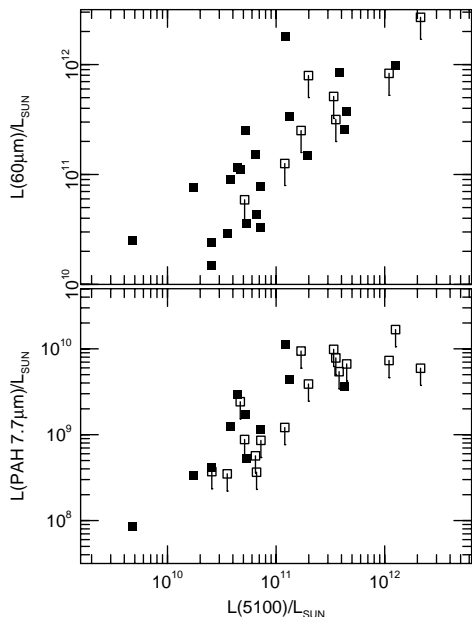


FIG. 5.— Top: The correlation of the optical (5100Å) and FIR (60μm) continuum luminosities. Bottom:  $L(5100)$  vs.  $L(\text{PAH } 7.7\mu\text{m})$  showing detections (full squares) and upper limits (empty squares).

are not in a position to test this relationship for sources with  $L(5100) > 10^{12} L_{\odot}$ , we note the tendency of upper limits at the high- $L$  end of the diagram to fall below the relationship seen for the lower luminosities. This is now confirmed by the recent work of Maiolino et al. (2007) who studied much higher luminosity QSOs.

### 3. DISCUSSION

#### 3.1. Possible origins of the FIR emission

The present study extends the work of Sanders et al. (1989), Elvis et al. (1994), Kuraszekiewicz et al. (2003), Haas et al. (2003), R06 and others who studied the IR-SED of various subgroups of AGNs. Many of the spectra used to construct those SEDs are of sources that were either found in X-ray selected samples (e.g. the sources in Elvis et al. (1994) and Kuraszekiewicz et al. (2003)) or in UV selected samples (the PG samples of Sanders et al. (1989) and Haas et al. (2003)). Our QUEST sample is very similar to the Sanders et al. (1989) sample and also to the other samples containing UV selected X-ray bright QSOs. Two important differences are the small fraction of radio-loud sources in our QUEST sample (5 out of 29 QSOs compared with about 50% of the sources in Haas et al. (2003)) and the smaller range in optical luminosity (only two orders of magnitude). Despite the relatively small luminosity range, the diversity in spectral properties in our sample is large with a clear distinction between weak-FIR and strong-FIR sources (Fig. 4). Most important regarding the comparison with earlier works is the greater level of detail over the 6–35μm range where *Spitzer* IRS is clearly superior to previous instruments. In this respect our SEDs are superior to the (much larger number of) broad band R06 SEDs. This improved resolution results in the detections of previously unobserved PAH features (paper I), in a real correlation between  $L(\text{PAH } 7.7\mu\text{m})$  and  $L(\text{FIR})$  in QUEST QSOs, and in a more

detailed view of the shape and the strength of several MIR features, such as the silicate bumps centered at around 10 and 18μm.

A major goal of the present investigation is to isolate the AGN-powered IR spectrum of the QUEST QSOs. This requires an understanding of the origin of the FIR emission and a comparison with theoretical models that predict the expected dust emission under different conditions. There are a number of such models in the literature including those of Pier & Krolik (1992; 1993), Granato & Danese (1994), Efstathiou & Rowan-Robinson (1995), Nenkova et al. (2002) and Kuraszekiewicz et al. (2003). They address various possibilities regarding the dust distributions, the orientation of the central torus, and the overall geometry. In general, such models can be divided into two groups: those assuming a continuous gas distribution (all models except those of Nenkova et al.) and those assuming a clumpy dusty medium (Nenkova et al. (2002), see also Elitzur et al. (2004)). Examples of fits to observed IR spectra are shown in Kuraszekiewicz et al. (2003, models of the SEDs of three QSOs), Pier & Krolik (1993, see Fig. 5) and Nenkova et al. (2002, e.g. Fig. 3). Key issues in such models are the agreement with the observed NIR-MIR spectrum and the question of whether the FIR emission is due to the same central structure or whether it is produced, independently, by isolated kpc-scale star-forming regions in the host galaxy.

Kpc-scale luminous star forming regions have been proposed, in several papers, as the origin of the FIR radiation in QSOs and in lower luminosity Seyfert galaxies (e.g. Rowan-Robinson 1995; Barthel 2006). Haas et al. (2003) address this possibility in their comprehensive investigation of a sample of 47 PG QSOs which covers about three orders of magnitude in optical continuum luminosity. In particular, they provide estimated dust temperatures that are required to explain the observed FIR spectrum of all sources. These estimates are based on broad band measurements of the 20–100μm continuum and suggest a typical dust temperature of 30–50 K for most sources, similar to the range found for nearby ULIRGs by Klaas et al. (2001). According to Haas et al. (2003), the high redshift highest luminosity sources in the sample exhibit a warmer IR continuum that peaks in the MIR part of the spectrum. In such sources, the entire 50–150μm part of the spectrum is interpreted as the Rayleigh-Jeans tail of an AGN-heated dust component. Haas et al. (2003) further searched for PAH emission in those sources. While they did not have any detections, they commented on the fact that the derived upper limits are consistent with the assumption that the entire FIR luminosity is of starburst origin, except for the few most luminous QSOs in their sample.

Further general support for the likely SF origin of the FIR emission comes from the correlation of radio and infrared properties. According to Haas et al. (2003), the observed  $L(1.4 \text{ GHz})/L(\text{FIR})$  ratio in radio quiet QSOs (about 50% of the sources in their sample) is very similar to the ratio observed in starburst galaxies (Condon 1992), where the FIR emission is due to starburst heated dust, and the radio emission due to supernovae is proportional to the star formation rate. Radio-loud QSOs contain an additional, more powerful radio source which is associated with the compact active core of the AGN. The Condon (1992) relation applied to our sample seems to provide a firm lower limit to the radio emission of all PG quasars. This strengthens the assumption that powerful star formation is taking place in most, and perhaps all such sources.



Given all this, we proceed to discuss two different scenarios. The first involves two separate IR sources: an inner structure that emits the 1–40  $\mu\text{m}$  continuum and a surrounding SF region that emits the FIR continuum and the associated PAH emission features. The second requires only one large dusty structure that produces the entire IR spectrum by absorption and re-emission of the primary source radiation at different distances. Along the way we also discuss caveats related to the expected range in  $L(\text{FIR})/L(\text{PAH})$ .

### 3.2. The intrinsic SED of type-I AGNs

#### 3.2.1. Starburst produced FIR continuum

We first consider the possibility that the infrared SED of the QUEST QSOs contains two distinct components: one originating in a dusty central structure and the other in extended SF regions. As shown in paper, the QUEST observations are consistent with the assumption that at least one third, and perhaps almost all the FIR emission is due to starbursts. Given 100% starburst contribution we find that the starburst luminosity in our sample is between  $1.6 \times 10^{10}$  to  $2.5 \times 10^{12} L_{\odot}$  and the corresponding (somewhat model dependent) star formation rate is between about 2 and 300 solar masses per year. We caution that the results presented below may not apply outside the luminosity range considered here. Thus sources like those observed by Haas et al. (2003), that are an order of magnitude more luminous than the most luminous QUEST QSOs, may contain a different combination of warm AGN-heated and cold starburst-heated dust.

We proceed to produce a template starburst SED that will be subtracted from the spectra of all the QUEST QSOs. The best estimate for such a template is the mean spectrum of the 12 starburst dominated ULIRGs in our QUEST sample that do not show AGN indicators like strong mid-IR continuum or high excitation lines like [Ne V] or [O IV] and also do not show strong MIR absorption (the SB-ULIRG group also discussed in paper I §4.1). The detailed properties of those 12 ULIRGs will be discussed in a future paper, here we only use their composite spectrum. This choice is preferable to the use of templates based on observations of nearby starburst galaxies since these are not only different in their starburst properties but are also subjected to aperture, metallicity and luminosity effects.

Our starburst dominated ULIRG template was obtained by normalizing the 12 spectra to have the same 60  $\mu\text{m}$  flux and then taking the mean at every wavelength. The individual spectra show modest spread around the mean for all  $\lambda > 5 \mu\text{m}$ , which is the part of the spectrum relevant for our analysis. This starburst dominated ULIRG template was subtracted from the two mean QSO spectra (weak and strong FIR emitters), with a scaling consistent with the assumption that most of the 50–100  $\mu\text{m}$  emission is due to star formation. The normalization that was adopted made the long wavelength part of the residual spectrum, after subtraction (i.e. the part assumed to be the intrinsic AGN SED), consistent with optically thin dust emission. The presence of such an optically thin AGN dust component is unambiguously indicated by the silicate emission features. We have used optically thin dust models that were computed for fitting the silicate emission in QUEST QSOs (Schweitzer et al., in preparation). This method dictated the fractional amount of starburst contribution at those wavelengths albeit with a rather large uncertainty. It resulted in  $\sim 87\%$  due to starbursts at 60  $\mu\text{m}$  for the strong FIR case and  $\sim 80\%$  for the weak FIR case. Fig. 6

shows the two mean QSO spectra before and after this subtraction. The adopted starburst template is consistent with the  $L(\text{PAH } 7.7 \mu\text{m})/L(\text{FIR})$  correlation for QSOs (Fig. 4 of paper I) and the similarity of PAH 7.7  $\mu\text{m}$ /FIR ratios in PG QSOs and star-bursting ULIRG stated there. The scaling is also independently supported by the absence of PAH residuals in the subtracted spectra of Fig. 6. We thus obtain “intrinsic AGN” SEDs for each of the two groups.

The assumption that most of the FIR emission is due to a starburst component results in a clear drop of the computed AGN SED at long wavelengths. While the exact  $\lambda > 30 \mu\text{m}$  slope of depends on the adopted scaling, a clear decay in  $\lambda F_{\lambda}$  beyond 30  $\mu\text{m}$  cannot be avoided without leaving significant PAH residues which would indicate failure to subtract star formation. In contrast, our intrinsic AGN SEDs show only some [Ne VI] 7.6  $\mu\text{m}$  emission left on top of the continuum in the 6–8  $\mu\text{m}$  region. As evident from Figs. 1 and 6, almost all of our sources, and the two median SEDs, contain noticeable silicate features that must originate in optically thin regions of dust emission. The inferred long wavelength drop of our intrinsic AGN SED is consistent with this component since it suggests a slope which is steeper than a blackbody slope. A flatter SED (in particular for the FIR-strong sources) would require an alternative explanation.

Inspection of Fig. 6 reveals a high degree of similarity between the intrinsic AGN SEDs of weak and strong FIR emitters. They both show a relatively flat spectrum in  $\lambda L_{\lambda}$  with three distinct “bumps”: two corresponding to the silicate features at 10 and 18  $\mu\text{m}$ , and a third which is centered at around 3  $\mu\text{m}$ . The average SED of the sources with FIR upper limits is also in agreement with the two mean SEDs over the wavelength range where it is available, and also shows the same three bumps. Table 2 lists the intrinsic 1–40  $\mu\text{m}$  spectrum of the weak FIR group in normalized flux units.

The short wavelength feature has been noted in various earlier papers, most recently by Glikman et al. (2006, see references to earlier work in this paper) who could only observe the short wavelength side of the feature and modeled it as a combination of a nonthermal powerlaw and a 1260 K blackbody. It extends from below 1  $\mu\text{m}$  (the “1 micron inflection” in R06) to about 5–8  $\mu\text{m}$  and is better seen in our new SEDs because of the much clearer view of the 5–10  $\mu\text{m}$  part of the spectra, where the long wavelength upturn of this feature is included in the *Spitzer* spectral range. We interpret this feature as the signature of the hottest dust in the AGN inner structure, at a temperature of 1000–1500 K. Obviously, a realistic torus will radiate over a range of temperatures. We also caution that there is a relatively wide range, and a large scatter, among the individual sources of our sample in this part of the spectrum and some of the data (e.g. the L-band photometry) are incomplete. Given this, the difference between the two intrinsic SEDs presented here is surprisingly small.

In summary, the SF-dominated scenario for the FIR implies similar AGN SEDs for all sources, showing three distinct NIR-MIR humps and very similar long wavelength ( $\lambda > 20 \mu\text{m}$ ) slopes. Such a slope is consistent with the observed silicate features and can be attributed to the absence of large amounts of AGN-heated dust with temperatures below about 200K.

#### 3.2.2. AGN-produced FIR continuum

An alternative view is that direct AGN heating, followed by re-radiation of cool distant dust, is the origin of a large fraction of the observed FIR emission. Such scenarios have been

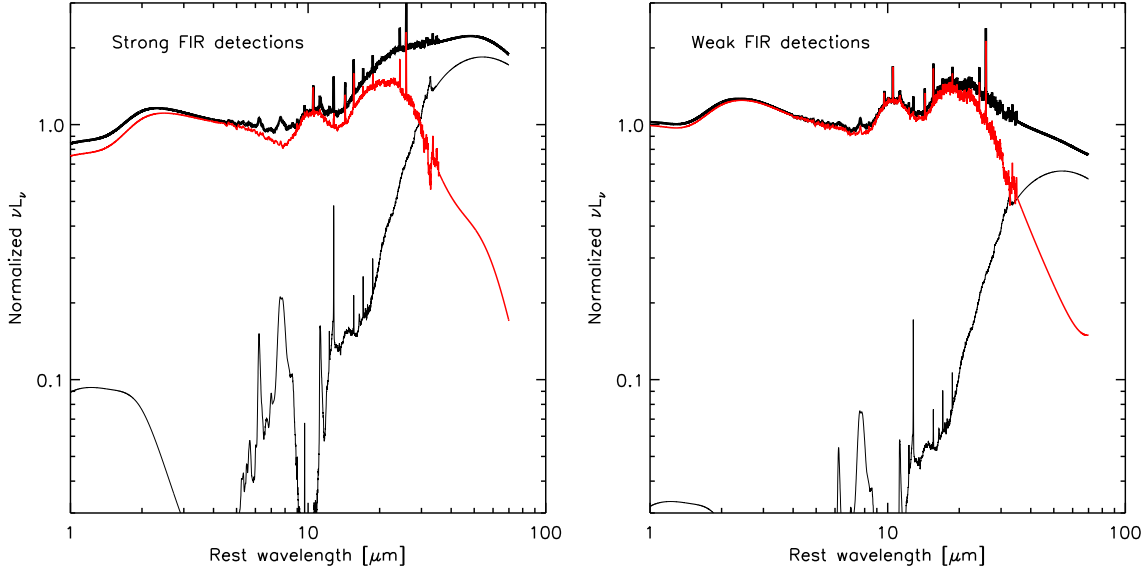


FIG. 6.— Normalized mean SEDs for strong FIR QSOs (left, top curve) and weak FIR QSOs (right, top curve). The adjacent red SED curves show “intrinsic” AGN SEDs obtained by the subtraction of the scaled mean starburst (ULIRG) spectrum (shown in black) from the mean SEDs. (See text for explanation).

TABLE 2  
AVERAGE QSO SEDS

Rest Wavelength $\mu\text{m}$	Observed QSO SED $\lambda F_{\lambda}$ (arb.units)	Intrinsic AGN SED for FIR-weak QSOs $\lambda F_{\lambda}$ (arb.units)
1.202	0.944	0.974
1.216	0.944	0.973
1.230	0.945	0.972
1.245	0.946	0.972
1.259	0.947	0.971
1.274	0.948	0.971
1.288	0.949	0.971
1.303	0.951	0.971
1.318	0.953	0.971
1.334	0.956	0.972
1.349	0.959	0.973

NOTE. —

Col. (1) — Rest wavelength

Col. (2) — Average observed SED of 28 PG QSOs (see Fig. 3 top, smoothed)

Col. (3) — Average intrinsic AGN SED of 8 ‘FIR-weak’ PG QSOs, after subtraction of a starburst component (see Fig. 6 right, smoothed)

Full SEDs are given in an electronic table.

discussed in several earlier papers including Sanders et al. (1989) and Haas et al. (2003). Successful models of this type must explain the required range of dust temperatures as well as the FIR luminosity and the strength of the PAH emission. In this case, the differences between strong-FIR and weak-FIR emitters reflect a range in dust temperature. For sources of similar primary luminosity, differing SEDs imply different dimensions and/or geometry of the inner dusty structure.

For the QSOs under study, the FIR luminosity is comparable to  $L(5100)$  which, in turn, represents some 15% of the bolometric luminosity (§2.4) (the ratio has a weak dependence on  $L(5100)$  that we ignore here). Thus  $L_{12} \simeq 7L_{12}(\text{FIR})$ , where  $L_{12}$  and  $L_{12}(\text{FIR})$  are the bolometric (primary) and FIR luminosities in units of  $10^{12} L_{\odot}$ , respectively. In general, continuous dust distribution models, such as those published by Pier & Krolik (1993), would fail to produce such a large FIR luminosity since the assumed torus geometries result in a strong attenuation of the central source radiation at large distances. A somewhat different geometry, of a flaring or warped

disk, can solve the FIR energy budget problem but introduces a related problem of extremely large dimensions. This is easily understood if we consider the case of a dusty region which is fully exposed to the central source of radiation. In such gas

$$T_{\text{dust}} \simeq 1500 r_{\text{pc}}^{-t} L_{12}^{1/4} \text{ K}, \quad (1)$$

(e.g. Phinney 1989) where  $r_{\text{pc}}$  is the distance from the central source in pc and  $t = 2/(4 + s)$ . For optically thick dust  $s = 0$  and for other cases it describes the frequency variation of the dust cross section ( $\sigma_{\lambda} \propto \lambda^{-s}$ ). For most cases of interest  $s = 1 - 2$ .

The present scenario suggests that the 50–100  $\mu\text{m}$  emission of the QUEST QSOs is mostly from dust with  $T_{\text{dust}} \simeq 40 - 65$  K. For a typical low luminosity source in our sample  $L_{12} \simeq 0.2$ , which for the optically thick case with  $T_{\text{dust}} = 50$  K gives  $r \simeq 0.4$  kpc. For optically thin dust with  $s = 1.5$  we get  $r \simeq 1.7$  kpc. The derived dimensions for the highest luminosity QUEST QSOs, with  $L_{12} \sim 17$ , are an order or magnitude or more larger.

Given the inferred dimensions, and the fraction of the bolometric luminosity absorbed by the dust, we find that the distant dusty gas in the most luminous QUEST QSOs must rise to a height of at least 0.6 kpc, and perhaps much higher, above the galactic plane. Such a huge structure must have unusual dynamical consequences and is not consistent with a stable, relaxed system. The limitations are probably less severe in interacting systems where warped galactic disks may be involved. The solid angle in this case can be considerably larger, especially during the later phases of the merger.

The clumpy models of Nenkova et al. (2002) come closer to the observed dimensions since, in those cases, nearby clumps can contribute to the IR emission from their hot (illuminated) as well as their cold (back-side) faces. In such cases, the dimensions can be smaller and the only firm lower limit on  $r_{pc}$  is obtained from simple blackbody considerations. For a partially filled radiating spherical surface of solid angle  $\Omega$ ,  $r_{pc} \simeq 2.7 \times 10^6 T_{dust}^{-2} L_{12}^{1/2} (FIR) \Omega^{-1/2}$ . Assuming  $T=50$  K and guessing  $\Omega/4\pi \simeq 0.2$ , we get in this case, for the most luminous QUEST QSOs, a radius of about 1 kpc.

The critical challenge for the cool AGN-heated dust scenario is the presence of strong PAH emission features in many of our QSOs and in the average SEDs, which are so naturally associated with the FIR emission if the latter is assumed to be due to star formation. This is independent of the assumed dimension of the cool dust region. However, the exact amount of starburst produced FIR emission requires more discussion. In particular, the specific  $L(FIR)/L(PAH)$  ratio observed in star forming ULIRGs and adopted here naturally leads to the scenario of starburst dominated FIR emission discussed in the previous section. However, this ratio is known to depend on the conditions in the ISM and can be, in some cases, significantly lower than the one assumed here. This is known to be the case in quiescent ‘cirrus-type’ hosts. In the extreme case of  $\sim 10$  times lower  $L(FIR)/L(PAH)$  ratio (known for some quiescent disks) a flat or a rising intrinsic AGN continuum out to FIR wavelengths remains possible. Cirrus type conditions cannot be excluded for the low PAH and FIR luminosity members of our sample which overlap with luminosities of quiescent galaxies (paper I), but become progressively unlikely at high star forming luminosities in the LIRG and ULIRG regime. More support for ULIRG-like FIR to PAH ratio in QSO hosts is given by the recent finding of a ULIRG-like ratio in the  $\sim 5$  times more luminous Cloverleaf QSO (Lutz et al. 2007), where the observed  $L(PAH)$  is much higher than in known quiescent disks.

Considerations of cirrus emission add to the uncertainty on the  $\lambda > 30\mu m$  slope of the intrinsic AGN SED derived in the previous section. They clearly leave the possibility of a flatter long wavelength slope for the QSOs with lower  $L(PAH)$  and  $L(FIR)$ . Most of these sources belong to our FIR-weak group with a global SEDs which is already falling gently at longer wavelengths. Thus, a dropping FIR component must also be present in the intrinsic AGN SED even if  $L(FIR)/L(PAH)$  is smaller than the one assumed here. As for those sources with larger  $L(PAH)$  and  $L(FIR)$ , the assumed ULIRG-like ratio is favored because of the similar luminosity to the QUEST ULIRGs. Here again the intrinsic AGN SED must be falling at long wavelengths but with a considerable uncertainty on the slope.

To summarize, the assumption of AGN dominated FIR emission then requires a solution to both the PAH and dimension problems. It would also require an explanation for the al-

most identical ratios between  $L(FIR)$  and  $L(PAH 7.7\mu m)$  observed in our QUEST QSOs and in ULIRGs (paper I). We therefore consider the assumption of a starburst dominated FIR emission to be more plausible for the PG QSOs discussed here. For QSOs with a larger ratio of AGN to host luminosity, the intrinsic AGN SED may dominate the emission out to longer wavelengths.

### 3.3. The AGN-starburst connection at low and high redshift

The observations shown in Fig. 5 clearly suggest significant correlations between the primary AGN continuum and the starburst produced emission (given our preferred explanation for the origin of the FIR emission). This was already pointed out in paper I where similar correlations relating e.g.  $L(6\mu m)$  and  $L(60\mu m)$  were shown. This is of considerable theoretical interest since current galaxy and BH evolution models do not predict a specific trend and only describe a general evolutionary relationship which is not necessarily coeval. Such models, that are based on detailed numerical simulations (e.g. Hopkins et al. 2006; Volonteri et al. 2006; Granato et al. 2004) calculate the star formation rate and the BH growth rates as functions of cosmic time yet they definitely allow a time lag between the end of star formation and the commencement of black hole activity. Our observations of the QUEST sample do not require such a delay at redshifts 0.1–0.3. The sample may not represent all AGNs but it gives a fair representation of unobscured sources at those redshifts. This may indicate that enhanced SF activity, when present, includes the very central part of the galaxy. Thus, some of the starburst produced gas can find its way to the vicinity of the BH on a time scale which is short compared to the life time of the global, galactic scale starburst activity. More complicated scenarios including the obscured and unobscured phases of a certain source (e.g. Hopkins et al. 2006) are also possible.

A similar phenomenon may well be occurring at redshifts much larger than 0.3. Deep sub-mm and mm photometry has led to the detection of rest frame submm and far-infrared dust emission from radio-quiet quasars at redshifts up to 6.42 (e.g. Omont et al. 2001; Isaak et al. 2002; Bertoldi et al. 2003). Indirect arguments, like CO measurements, have been used to suggest that this emission is powered by star formation, implying that these quasars coexist with extremely powerful  $\gtrsim 10^{13} L_{\odot}$  starbursts. If the PAH to FIR emission in these QSOs is similar to the one in ULIRGs, detection of PAH on top of a strong continuum may be within the reach of *Spitzer* spectroscopy. PAH emission from similar luminosity SMGs has been shown to be detectable, e.g. Lutz et al. (2005). Clearly, the extrapolation of the relationships found here to higher redshift, higher luminosity AGNs depends on the ability to detect PAH features in such sources. There are already some interesting upper limits in several extremely luminous QSOs (Maiolino et al. 2007) and a real detection in a high redshift high luminosity QSO with a strong millimeter flux (Lutz et al. 2007).

Having measured the  $L(5100)-L(FIR)$  relationship, we can estimate the relative growth rate of the central BH and the galactic bulge, assuming all the observed star-forming activity contributes to the growth of the bulge. For the QUEST QSOs,  $L(FIR)/L_{bol} \simeq 0.15$ . Assuming a BH accretion efficiency  $\eta$ , we can convert the (primary) bolometric luminosity to BH mass growth rate and the observed FIR luminosity to star formation rate. This gives  $g(bulge)/g(BH) \sim 20(\eta/0.1)$  where  $g$  stands for growth rate. This is more than an order of magnitude smaller than that required to explain the locally observed

bulge and BH mass ratio under the assumption of a similar duration for the two phenomena. Thus, the numbers presented here may indicate that the AGN activity phase is, on the average, an order of magnitude shorter than the star-formation phase. It would be interesting to carry out a similar analysis for higher redshift, higher luminosity AGNs. For example, Steidel et al. (2002) suggest AGN fractions of about 3% in  $z \sim 3$  UV-selected samples, not very different from what was found here.

#### 4. CONCLUSIONS

The main conclusion of the present work, and of paper I, is that most and perhaps all of the FIR luminosity of the QUEST QSOs is due to starburst activity. This conclusion is based mostly on the tight correlation between the luminosity of the PAH  $7.7\mu\text{m}$  feature and the FIR luminosity. As explained in §3, there are alternative relationships for  $L(\text{FIR})/L(\text{PAH})$  that are different from the ones used here but these we consider inapplicable to the objects in question. While there are clear PAH  $7.7\mu\text{m}$  detections in only 11 of the sources studied here, most of the derived upper limits, as well as the composite spectrum of all sources *not showing* clear PAH emission, are consistent with this assumption (paper I). In this scenario, the starburst luminosity in our sample is between  $1.6 \times 10^{10}$  to  $2.5 \times 10^{12} L_{\odot}$  corresponding to star formation rates of about 2 and 300 solar masses per year. The upper lu-

minosity range is close to the luminosity of the most luminous starburst-dominated ULIRGs in our sample.

The assumption that most of FIR luminosity is due to starburst activity allows us to estimate the minimum temperature of the AGN heated dust in the central dusty structures of our QSOs. This temperature is of order 200 K. The inferred maximum dimensions of the torus in the simplest, continuous gas distribution case is of order  $100 L_{12}^{1/2}$  pc, in reasonable agreement with all available observations.

Finally, our work shows that observed AGN SEDs can be misleading showing shapes that are quite different from the intrinsic SED. We suggest that future AGN models that try to reproduce the NIR-FIR spectrum of type-I sources use the results presented in Fig. 6 and Table 2 as a more realistic representation of the intrinsic AGN spectrum.

We thank Todd Boroson for kindly allowing us to use his optical data for PG quasars. We thank Amiel Sternberg for discussions and comments on the manuscript. Funding for this work has been provided by the Israel Science Foundation grant 232/03. SV, DSR, and DCK were supported in part by NASA contract 1263752 issued by JPL/Caltech. HN acknowledges a Humboldt foundation prize and thanks the host institution, MPE Garching, where most of this work was performed.

#### REFERENCES

- Barthel, P.D. 2006, A&A, 458, 107  
 Bertoldi F., Carilli, C.L., Cox, P., Fan, X., Strauss, M.A., Beelen, A., Omont, A., Zylka, R. 2003, A&A, 406, L55  
 Boroson, T.A., Green, R.F. 1992, ApJS, 80, 109  
 Condon, J.J. 1992, ARA&A, 30, 575  
 Efsthathiou, A., Rowan-Robinson, M. 1995, MNRAS, 273, 649  
 Elitzur, M., Nenkova, M., & Ivezić, Z. 2004, ASP Conf. Ser. 320: The Neutral ISM in Starburst Galaxies, 320, 242  
 Elvis, M., et al. 1994, ApJS, 95, 1 (E94)  
 Genzel, R., et al. 1998, ApJ, 498, 579  
 Genzel, R. & Cesarsky, C. J. 2000, ARA&A, 38, 761  
 Glikman, E., Helfand, D. J., & White, R. L. 2006, ApJ, 640, 579  
 Granato G.L., Danese, L., 1994, MNRAS, 268, 235  
 Granato, G.L., de Zotti, G., Silva, L., Bressan, A., Danese, L. 2004, ApJ, 600, 580  
 Haas, M., et al. 2003, A&A, 402, 87  
 Hatziminaoglou, E., et al. 2005, AJ, 129, 1198  
 Hopkins, P. F., Hernquist, L., Cox, T. J., Di Matteo, T., Robertson, B., & Springel, V. 2006, ApJS, 163, 1  
 Hyland, A.R., Allen, D.A. 1982, MNRAS, 199, 943  
 Isaak, K.G., Priddey, R.S., McMahon, R.G., Omont, A., Peroux, C., Sharp, R.G., Withington, S. 2002, MNRAS, 329, 149  
 Jarrett, T. H., Chester, T., Cutri, R., Schneider, S., Skrutskie, M., & Huchra, J. P. 2000, AJ, 119, 2498  
 Kaspi, S., Maoz, D., Netzer, H., Peterson, B.M., Vestergaard, M., Jannuzi, B.T. 2005, ApJ, 629, 61  
 Klaas, U., et al. 2001, A&A, 379, 823  
 Kuraszkiewicz, J. K., et al. 2003, ApJ, 590, 128  
 Lacy, M., et al. 2004, ApJS, 154, 166  
 Lutz, D., Valiante, E., Sturm, E., Genzel, R., Tacconi, L.J., Lehnert, M.D., Sternberg, A., Baker, A.J., 2005, ApJ, 625, L83  
 Lutz, D., et al. 2007, (ApJ, in press, arXiv:0704.1559)  
 Maiolino, R et al., 2007 (A&A in press, arXiv:0704.0133)  
 Marconi A., Risaliti, G., Gilli, R., Hunt, L.K., Maiolino, R., Salvati, M. 2004, MNRAS, 351, 169  
 McAlary, C.W., McLaren, R.A., McGonegal, R.J., Maza, J. 1983, ApJS, 52, 341  
 Nenkova, M., Ivezić, Ž., & Elitzur, M. 2002, ApJ, 570, L9  
 Netzer, H., Trakhtenbrot, B. 2007, ApJ, 564, 754  
 Neugebauer, G., Green, R.F., Matthews, K., Schmidt, M., Soifer, B.T., Bennett, J. 1987, ApJS, 63, 615  
 Omont, A., Cox, P., Bertoldi, F., McMahon, R.G., Carilli, C., Isaak, K.G. 2001, A&A, 374, 371  
 Phinney, E. S. 1989, NATO ASIC Proc. 290: Theory of Accretion Disks, 457  
 Pier, E. A., & Krolik, J. H. 1992, ApJ, 399, L23  
 Pier, E. A., & Krolik, J. H. 1993, ApJ, 418, 673  
 Richards, G.T, et al, 2006, ApJS, 166, 470 (R06)  
 Rowan-Robinson, M. 1995, MNRAS, 272, 737  
 Sanders, D.B., Phinney, E.S., Neugebauer, G., Soifer, B.T., Matthews, K. 1989, ApJ, 347, 29  
 Schweitzer, M., et al. 2006, ApJ, 649, 79  
 Scott, J.E., Kriss, G.A., Brotherton, M., Green, R.F., Hutchings, J., Shull, J.W., Zheng, W. 2004, ApJ, 615, 135  
 Shemmer, O., Netzer, H., Maiolino, R., Oliva, E., Croom, S., Corbett, e., di Fabrizio, L. 2004, ApJ, 614, 547  
 Steidel, C. et al. 2002, ApJ, 576, 653  
 Sturm, E., Lutz, D., Verma, A., Netzer, H., Sternberg, A., Moorwood, A.F.M., Oliva, E., Genzel, R. 2002, A&A, 393, 821 (S02)  
 Trammell, G. B., Vanden Berk, D. E., Schneider, D. P., Richards, G. T., Hall, P. B., Anderson, S. F., & Brinkmann, J. 2006, ArXiv Astrophysics e-prints, arXiv:astro-ph/0611549  
 Voit, G. M. 1992, ApJ, 399, 495  
 Volonteri, M., Salvaterra, R., & Haardt, F. 2006, MNRAS, 373, 121